Low-Field ^{1}H NMR Study on Geopolymers: the Effect of Paramagnetic Fe(III)

Ziyou Yu[a], Rodrigo de Oliveira-Silva[a], Yiannis Pontikes[b], Dimitrios Sakellariou[a, *]

[a]*KU Leuven, M2S, cMACS, Celestijnenlaan 200F, 3001 Leuven, Belgium*

[b]*KU Leuven, Department of Materials Engineering, Kasteelpark Arenberg 44, 3001 Leuven, Belgium*

Abstract:

Geopolymers are inorganic polymers with 3D framework structures having superior mechanical and physical properties. Metakaolin-based geopolymers synthesized using solutions of Fe(III) chloride have been studied *ex-situ* and *in-situ* using low-field ^{1}H nuclear magnetic resonance (LF NMR). The results revealed that the introduced Fe(III) could affect the spin relaxation and the pore structure. The effect on spin relaxation was determined by quantifying the relation between surface relaxivities and Fe(III) ion content. The effect on pore size was measured by Mercury Injection Capillary Pressure (MICP), showing a two-stage evolution. The pore size increased slightly before and dramatically after

the threshold of 2.0 wt% iron content. We propose herein as possible causes the reaction between hydroxide ions and Fe(III) and the formation of Si(Al)-Fe-oxyhydroxides. During the early (first three days) polymerization of geopolymers the *in-situ* T_2 curves revealed three stages (i.e, dissolution, condensation, and stabilization) which are affected to different degrees by Fe(III).

Keywords: NMR paramagnetism; ^{1}H NMR relaxation; geopolymers; pore size; T_1 and T_2 nuclear relaxation times.

1. Introduction

Geopolymers, a term coined first by Davidovits[1], are inorganic materials composed of a tri-dimensional aluminosilicate framework and potential alternatives to Ordinary Portland Cements (OPCs)[2]. Geopolymers include a large volume of micro and mesopores[3, 4], with an average pore radius smaller than 20 nm[4, 5]. The nano-porous structures in geopolymers prevent ion diffusion and penetration towards the reinforcement bars in concrete[6], which acts like a protective mechanism for the bar and therefore prolongs the service life of the material. In the past decades, several techniques, such as scanning electron microscopy (SEM-BSE) image analysis[7], mercury injection capillary pressure (MICP)[8], (ultra) small-angle X-ray or neutron scattering (SAXS-USAXS, SANS)[4], and low-field nuclear magnetic resonance (LF NMR) relaxometry[9, 10], have been emerged to determine porosity and pore size distributions in porous materials. The former two techniques have limitations in estimating micro-pores due to the micro-cracking occurring under vacuum[11] and pore structure deformation occurring under high pressure[12]. The scattering methods can provide information about the open/closed porosity[4] and pore size distribution[13], but the primary disadvantages concern the low accessibility of expensive synchrotron radiation, neutron and x-ray sources. LF NMR relaxometry is a low-cost and accessible benchtop technique providing non-invasive, non-destructive analysis by recording *in-situ* the porous structure dynamics

over time. In this work, a homemade 0.3 T NMR relaxometer (13.24 MHz ^{1}H Larmor frequency) was applied to all the experiments.

Over the years the applications of LF NMR relaxometry in porous construction materials have included the determination of pore size distribution [10,14], the characterization of molecular absorption in hardened cement pastes [15], and the investigation of the dynamic changes of porous structures during the early stage of curing [16] (first couple of days depending on the material). These applications were achieved by measuring longitudinal relaxation time (T_1) and transverse relaxation time (T_2) distributions, 2D T_1-T_2 correlations, and the evolution of T_2 over time. NMR T_1 and T_2 relaxation is caused by the fluctuations in the local magnetic field surrounding the observed nuclei. In porous media studied at low magnetic fields, the nuclear spin relaxation phenomenon of guest molecules inside the pores is due to three relaxation mechanisms: 1) bulk relaxation, which is the intrinsic relaxation of the pure fluid and is determined by the physical/chemical fluid properties (e.g. viscosity and molecular size), 2) surface relaxation, which is due to the interactions between the fluid molecules and the atoms of the pore surface, and 3) molecular self-diffusion, which is causing magnetization dephasing because of the internal magnetic field gradients[17, 18] [19]. Because the bulk relaxation is very long, it can be ignored when there are also surface relaxation and molecular diffusion. When the diffusion is quick enough so that the molecules feel an average relaxation effect (from the bulk and the surface), there will be one single average relaxation value. This is the so-called ‘fast-diffusion’ limit. In this case, the contribution of relaxation

from molecule diffusion can also be ignored. As we shall see, the geopolymers possess small pores (in the scale of tens of nanometers), indicating that the relaxation is surface limited (in the case of 'fast-diffusion'). The source of the fluctuation of the local fields is mainly the proton-proton dipole coupling. However, the raw materials for geopolymer synthesis may also contain some paramagnetic impurities, such as Fe_2O_3[22-25]. Besides, iron can be a major component in industrial residues such as Fe-rich precursors, non-ferrous metallurgy slags and bauxite residues which have recently attracted great interest in views of valorisation[26]. In the presence of such iron paramagnetic ions, the proton-electron interactions result in much greater relaxation than proton-proton interactions on the pore surface, which may alter the surface relaxivity[27].

Considering the paramagnetic effects, Kleinberg *et al.*[28] and Foley *et al.*[27] have developed the theoretical NMR relaxation model of fluids inside natural rocks and synthesized materials, respectively, based on the KST theory[29]. The longitudinal, $\frac{1}{T_1}$, and transverse, $\frac{1}{T_2}$, relaxation rates can be expressed as:

$$\frac{1}{T_1} = \left(\frac{Sh}{V}\right)\left(\frac{n_M}{T_{1M}}\right) = \rho_1 \left(\frac{S}{V}\right)_{pore} \quad (1)$$

$$\frac{1}{T_2} = \left(\frac{Sh}{V}\right)\left(\frac{n_M}{T_{2M}}\right) = \rho_2 \left(\frac{S}{V}\right)_{pore} \quad (2)$$

where S and V are the surface area and the volume of the pore, h is the thickness of a monolayer of water and n_M is the proportion of surface sites occupied by paramagnetic ions, e.g., Fe(III). T_{1M} and T_{2M} are the relaxation times of a liquid molecule coordinated to a magnetic site on the surface, which are determined by the microscopic interaction between a nuclear spin on the fluid molecule and an electron spin on the magnetic ion on the solid surface and they are considered to be constants. ρ_1 and ρ_2 are the surface relaxivities and can be expressed as $\rho_{1,2} = \frac{hn_M}{T_{1M,2M}}$.

Equations (1) and (2) indicate that spin relaxation rate is determined by pore size and surface relaxivity. The surface relaxivity is highly dependent on the number of paramagnetic impurities on the pore surface. Although the pore size stays the same, the relaxation rate may vary due to the variation in paramagnetic concentrations[30], making it more complicated to interpret the LF NMR measurements. It becomes therefore essential to understand how the paramagnetic ions on the solid surface affect the T_1 and T_2 relaxation times and the surface relaxivities, ρ_1 and ρ_2.

The theoretical work on the NMR relaxation of fluids on solid surfaces has been well developed. However, the published experimental LF NMR studies are limited and somewhat unsystematic. Most of the literature work looked at the influence of the paramagnetic species on 1D relaxation time distributions (either T_1 or T_2[20, 31]), and only marginally on 2D T_1 -T_2 correlations and the T_1/T_2 ratio. To the best of our knowledge one article describes the use of 2D T_1 -T_2 correlation experiments [30, 32], and has

provided the possibility to obtain further insights. Furthermore, the curing process for construction materials is an important step affecting the structure development and strength of final products[33, 34]. LF NMR, as an *in-situ* method, has been applied to monitor the initial mixing period[16, 35] by observing the water evolution. This information is directly related to the setting process and the pore structure formation, which cannot be derived from other conventional viscosity and Vicat needle penetration methods[36]. Barberon *et.al* [37] have investigated a hydrated cement based mortar at different hydration times. They provided a new perspective based on the specific surface area evolution during the hydration. There was 1.17×10^{19} paramagnetic ion Fe(III) per grain in the dry sample. They observed the relaxation enhancement due to Fe(III) only at high frequency and above 10 hours of hydration. The influence of paramagnetic ion Fe(III) on the curing of geopolymer is, however, still unclear. Further research and systematic work would contribute to a better understanding and proper interpretation of NMR relaxation in porous materials, particularly, in the presence of paramagnetic ions.

Here we investigate the behavior of NMR relaxation of liquids inside pores of metakaolin (MK)-based geopolymers, loaded with different amounts of water soluble ferric chloride ($FeCl_3$), named soluble Fe(III) in the rest of the paper, to understand how the paramagnetic ions affects the T_1 and T_2 relaxation times and their ratio T_1/T_2. Instead of introducing non-soluble iron (in the form of iron oxide mechanically mixed with the MK)[38], we have chosen to add soluble iron ions (from $FeCl_3$ water solutions) because they are more likely to affect the formation and gel chemistry of the

geopolymer. By introducing Fe(III) ions into the MK-based geopolymer, we could also observe the influence of iron on the pore structure formation from LF NMR.

2. Experimental

2.1 Raw materials and sample preparation

High purity kaolinite was obtained from the clay minerals society, USA. The kaolinite was calcined at 750ºC for 7 hours to get metakaolin. X-ray diffraction (XRD) of the materials before and after calcination indicated no kaolinite residual. The chemical composition of metakaolin determined by X-ray fluorescence (XRF) (Table 1) was $1.9SiO_2 \cdot Al_2O_3$ with TiO_2 and Fe_2O_3 as the dominant impurities[39]. The Brunauer–Emmett–Teller (BET) surface area of metakaolin was 10.26 m^2/g, determined by N_2 adsorption on a 3Flex Physisorption instrument. The mean particle size, as detected on Beckman Coulter LS 13 320 particle size analyzer, was 2.9 μm, and 90 % of the particles were under 12.0 μm. The alkaline solution ($Na_2O \cdot SiO_2 \cdot 11H_2O$) was prepared by dissolving the NaOH pellets (Sigma-Aldrich, ≥98%) into diluted sodium tri-silicate solution (Water glass, Sigma-Aldrich, 99%) to reach Si/Na = 1 and Na/H_2O = 11. The solution was stored at 60 ºC for 24 hours before use so as it reaches the chemical equilibrium. Anhydrous ferric chloride (Sigma-Aldrich, 97%) was dissolved in deionized water to produce ferric chloride solutions with various mass concentrations, as additional iron sources to be added to the

MK-based system. The ferric chloride solutions were prepared just before the synthesis of the samples to avoid precipitation due to hydrolysis in water.

The experimental procedures included two series (Figure 1): (A) NMR experiments on cured samples and (B) *in-situ* NMR experiments on fresh samples. Both series started by mixing metakaolin with $FeCl_3$ solutions, followed by adding alkaline activators. The mixture was manually stirred for 15 min to give a paste with molar ratios of Al_2O_3/Na_2O=1 and Si/Al=3:2. The specific amount of each chemical can be found in Table 2. The samples were named MK0 to MK8, according to iron content going from low to high. The concentration of iron was calculated as the percentage of Fe(III) ions added to metakaolin. In the A-Series the paste was cast into a cylindrical silicone mold of 10 mm in both diameter and height, which matched the size of the sample holder in LF-NMR. The mold was tapped on the bench for 2 min to remove the entrained air. The samples were sealed with plastic film and cured for 20 h at 40 °C, followed by storage at ambient temperature and pressure for further characterization. The LF NMR measurements have been conducted on samples cured for the same duration (after storage for 7 days) to avoid the pore structure alteration. In the B-Series the mixed paste was directly loaded into the NMR sample holder (Teflon, cylinder with Ø10×10mm) and placed in the LF NMR chamber to start the *in-situ* experiments. The details of NMR experiments are described in the following section.

2.2 Low-field NMR experiments

The LF NMR experiments in the two series were conducted using a homemade 0.3 T NMR relaxometer. The magnetic field was produced by a homogeneous Halbach magnet. The magnet and sample were temperature-stabilized at 28 °C. The measurements were conducted at 13.24 MHz proton Larmor frequency using a solenoidal radiofrequency (RF) coil of 12 mm in diameter and 11 mm in length (11 turns). The pulse sequences that correspond to each experiment and parameters are shown in Figure 2. Longitudinal relaxation T_1 and transverse relaxation T_2 were acquired using inversion-recovery and CPMG sequences, respectively. The 2D T_1 - T_2 correlation experiments were carried out using a conventional inversion-recovery experiment detected during a CPMG pulse train. The monitoring of the evolution of the T_2 relaxation times was conducted by continuously recording CPMG experiment and storing the data every 90 seconds. By means of a 2D Laplace inversion, the distributions of T_1, T_2, and the 2D correlations between T_1 and T_2 were obtained.

In the A-Series (Figure 1), the geopolymer samples were vacuum saturated with deionized water for 8 hours. After removal from the deionized water bath, the samples were wiped with paper tissue to remove the excess water residing on the surface and were then transferred to the Teflon sample holder having a cap for LF-NMR measurements. The experiments for one sample (including T_1, T_2 relaxation and 2D T_1-T_2 correlation) could be

completed within 2 hours, so the water evaporation was negligible. In the B-Series, the freshly mixed paste was cast into the Teflon sample holder and placed inside the RF coil to start the *in-situ* T_2 dynamic experiment. The time was recorded from the end of mixing. The mass of the samples was calculated by weighing the sample holder before and after casting.T_2 relaxation time was recorded *in-situ* for 72 hours. The sample holder was weighted after the experiment and confirmed the weight loss due to water evaporation was less than 0.8%.

2.3 Complementary characterizations

X-ray diffraction of powdered samples was carried out with a Malvern PANalytical Empyrean diffractometer, using a CuKα radiation step size of 0.02º 2θ and a scan rate of 2 s per step. The scan range was 20 to 70° 2θ at 40 kV and 20 mA.

The mass magnetic susceptibility was determined using a magnetic susceptibility balance (MSB – AUTO, Sherwood Scientific Ltd). A finely powdered sample was placed in a standard sample tube (diameter 3.24 mm) above the minimum length (10 mm). The tube was tapped for 2 min to ensure the powder was dense. Mass and length of the sample were measured before putting the tube in the balance. The mass magnetic susceptibility was directly read from the balance.

The morphology of the cross-section of geopolymers was observed using scanning electron microscopy (SEM, FEI XL30 FEG). Geopolymers were coated with platinum to ensure conductivity.

The heat evolution during the curing was recorded in an isothermal conduction calorimeter (TAM Air device, TA Instruments).

Pore size distribution was determined by MICP with a mercury porosimeter (Micromeritics, USA). The bulk samples were deionized water-washed and vacuum dried at 40 ^{o}C for over 24 h before conducting the MICP measurements. A penetrometer with 5 bulb (cup) and a stem volume (capillary volume) of 0.392 cm^3 was applied to drive the used stem volume in the range of 70% to 90%[40]. Cyclic measurements (combined intrusion and extrusion steps) were conducted in the high-pressure range up to 415 MPa corresponding to a pore diameter down to 4 nm.

3. Results

3.1 X-ray diffraction

Figure 3 shows the XRD analysis for all the geopolymer samples. The XRD traces indicated the presence of an amorphous phase by the broad diffuse peak, together with weak peaks due to the TiO_2 (anatase) impurity (marked with * in Figure 3) originating from metakaolin (see Table 1). In the $FeCl_3$-loaded samples, crystalline NaCl appeared (depicted as ♦ in

Figure 3). The amount of NaCl was proportional to the concentration of $FeCl_3$. NaCl was considered to be one of the products due to the reaction between alkaline and ferric solutions. No XRD evidence of any crystalline Fe-rich phase was observed. Iron was, therefore, more likely to be present in an amorphous or poorly crystalline phase, beyond the detection capability of XRD. Similar results were observed in $Fe(NO)_3$-loaded metakaolin geopolymers[38].

3.2 Bulk magnetic susceptibility

To verify the paramagnetism introduced by the loading of $FeCl_3$ into the MK-based geopolymers, the samples were characterized by bulk magnetic susceptibility measurements. The results can be seen in Figure 4, where the iron content has also been recalculated as the mass ratio of Fe(III) in the final geopolymer samples (as shown in the upper x-axis). The obtained values of mass magnetic susceptibility were in the range of 2-30 $\times 10^{-7}$ emu/g, indicating all the samples were paramagnetic. A linear relation between mass magnetic susceptibility and iron content (dashed line in Figure 4) illustrates that as the iron content increases, the geopolymer becomes more paramagnetic in nature.

3.3 The effect of Fe(III) ions on pore sizes

The pore size distribution of MK-based geopolymers was determined by MICP. Figure 5(a) plots the median pore diameter (r_{50}) versus the loaded iron content. The r_{50} shows a slight increase in the range of 0 ~ 2.0 wt%

and a pronounced increase above 2.0 wt%, which can be fitted in a two-segment linear line (the dashed line in Figure 5(a)). The same trends (Figure 5(b)) also occur in T_1 and T_2 NMR "average" relaxation times (defined as the logarithmic mean values calculated from the T_1 and T_2 relaxation time distribution curves), which can correspond to pore radius according to Equations (1) and (2). The causes of pore size changes will be discussed in section 4.

3.4 The effect of Fe(III) ion on ^{1}H NMR relaxation

3.4.1 T_1/T_2 ratio

The T_1/T_2 ratio was calculated from the experimental T_1 and T_2 data, as shown in Figure 5(c). In sample MK0, the ratio is $\sim$2.55 and with increasing the iron content, it converges to $\sim$1.5, which is consistent with the results from Holthausen and Raupach[30]. Higher than 1 wt%, the indipendance of the T_1/T_2 ratio on iron content indicates that the iron content affects both ρ_1 and ρ_2 surface relaxivities to the same degree.

3.4.2 T_1 and T_2 relaxation

The T_1 and T_2 relaxation times are plotted versus Fe(III) concentration in Figure 5(b). Contrary to previous studies[30, 41], the T_1 and T_2 relaxation times did not decrease but increased with the introduction of Fe(III). The pore diameter also increased with Fe(III) content, which might be the

reason leading to longer relaxation times. The influence of Fe(III) on spin relaxation can be estimated from surface relaxivity (ρ). A variety of approaches have been proposed to characterize ρ, such as for example: NMR-MICP matching[42], NMR-BET correlation[43], NMR-SEM calibration[44]. In this study, MICP was applied to calibrate the surface relaxivity.

When assuming that the pore system is cylindrical, $\frac{S}{V}$ can be converted to $\frac{2}{R_t}$, where R_t is the throat radius[42]. Thus Equations (1) and (2) can be expressed as:

$$R_t = 2\rho_{e1,2}T_{1,2} \tag{4}$$

Where $\rho_{e1,2}$ are the effective surface relaxivities, which can be derived by maximizing the cross-correlation (CC) between the R_t and $T_{1,2}$ distributions[42]:

$$\mathrm{CC}(\rho_{1,2}) = \sum_i A_{Hg}(r_i) \cdot A_{NMR}(r_i = 2\rho_{e1,2}T_{1,2}) \tag{5}$$

where $A_{Hg}$is the intensity of R_t distribution, A_{NMR} is the intensity of $T_{1,2}$ distributions scaled by $2\rho_{e1,2}$. Note that this CC approach is valid for small pores in the fast diffusion limit. Strong diffusion between small and large pores requires to introduce more parameters, such as a coupling parameter proposed by Mesquita *et al* [42].

Figure 6(a) shows the values of ρ_1 and ρ_2 plotted against the iron concentration. ρ_1 and ρ_2 vary by about 1.5 times over the entire iron content range and can be described as linearly dependent on the iron content:

$$\rho_1(\mu m/s) = (0.40 \pm 0.24)\mathrm{Fe}[wt\%] + (4.93 \pm 0.61) \quad (6)$$

$$\rho_2(\mu m/s) = (0.74 \pm 0.52)\mathrm{Fe}[wt\%] + (9.81 \pm 1.62) \quad (7)$$

Figure 6(b) shows the ratio between ρ_2 and ρ_1, which is reduced rapidly with a small amount of iron and tends to be constant at higher iron contents. The trend is consistent with the T_1/T_2 ratio which was calculated directly from the LF NMR results.

To intuitively illustrate the influence of Fe(III) ions on spin relaxation, we can first consider two 'extreme' assumptions that only relaxivity or only pore size, depends on the iron content. The longitudinal relaxation time T_1 from experiment and calculation is plotted in Figure 7. The dotted line represents the effect of relaxivity only while keeping the pore size constant. The dashed line represents the effect of the pore size change while keeping the relaxivity constant. The constant pore size and relaxivity were taken from the MK0 sample. So both dotted and dashed lines represent the extremes for the T_1 relaxation times. A predicted T_1 relaxation time by multiplying the relaxivity function (Equation (6)) with the experimental

throat sizes (figure 5(a)) is represented by the solid curve and it is in line with the experimental data (squares).

Figure 7 confirms the combined effect of paramagnetism and pore size on the proton spin relaxation. Specifically, the introduction of paramagnetic ion (Fe(III)) causes the spin to relax faster (with a shorter T_1 and T_2), while the increase in pore radius due to the loading of Fe(III) ions make T_1 and T_2 longer. It can also be seen that when there are small changes in pore size (in the iron content range of 0 ~ 2.0 wt%), paramagnetism could have a great impact on spin relaxation. Conversely, once a huge increase occurs in the pore size (in the iron content above 2.0 wt%), the pore size rather than paramagnetism could affect spin relaxation more. When corresponding T_1 and T_2 to pore sizes, one should consider the surface relaxivity alteration in materials with different iron contents, even though the change in ρ seems very little compared to the change in pore size in this study. If the iron content is identical in different samples and can be treated as evenly distributed on the inner pore surface, ρ can also be considered constant, and the measured T_1 and T_2 can directly correspond to the pore sizes.

3.4.3 2D T_1-T_2 correlation

Another demonstration of the effect of Fe(III) ion on spin relaxation is may come from a 2D T_1-T_2 correlation experiment. Since T_1 is always longer than, or equal to T_2, in a 2D T_1-T_2 correlation map the NMR signal

will be visible only in one half of the plane, or at the diagonal ($T_1 = T_2$). In the case of water in confined pores, it is considered as in the fast-diffusion regime[19]. The relaxation behavior is determined by the surface chemistry and the concentrations of paramagnetic impurities on the pore surface[31, 32]. The T_1/T_2 ratio is theoretically independent of paramagnetic impurities[45]. The change of pore radius results in a movement of the signal down- or up-ward along a line parallel to the diagonal. Once the relaxation process is governed by bulk or diffusion relaxation, the signal will deviate from the line and T_1/T_2 decreases or increases accordingly.

The 2D T_1-T_2 correlations are shown in Figure 8(a)-(i). The dominant signal, lying between $T_1 = 2.0\ T_2$ and $T_1 = T_2$, belongs to confined pore water since T_2 relaxation time is in the range of 0.98 – 2.83 ms. The weak signal on the diagonal $T_1 = T_2$ associated with $T_{1,2} \approx 300$ ms is attributed to the absorbed water on the outer surface of the sample. The dominant signal in Figure 8(a) is close to $T_1 = 2.0\ T_2$, while in Figure 7(b) to (e), it moves towards the line $T_1 = \sim 1.5\ T_2$ (Figure 8(j)). This indicates that the relaxation contribution has changed from predominately geopolymer surface relaxation to iron dominated paramagnetic relaxation ($\rho_{1,2}$ increased). A tail is found in the signal in Figure 8(b) - (e) (the projection of the T_2 distribution), which is not observed in the 1D T_2 distribution. The tail of the T_2 distribution is probably related to the inhomogeneous distribution of Fe(III) ions on the inner pore surface, which results in the variation of ρ. The tail in Figure 8(f) - (i) disappeared, meaning that

ρ becomes homogeneous (the iron-bearing phase is homogeneous) or insignificant (the relaxation mechanism is no longer dominated by paramagnetic relaxation). If the former is the truth, the T_1/T_2 ratio should be about 1.5. However, T_1/T_2 decreases towards 1 according to Figure 8(j), indicating the relaxation process is governed by bulk relaxation. With increasing pore size, the dominant signal moves towards longer and progressively equal to each other relaxation times.

Note that the trend of T_1/T_2 with the iron content in the 2D T_1-T_2 measurement (Figure 8(j)) is dissimilar to the calculation from the 1D experiments (Figure 6(c)). It remains unclear what caused the difference. However, it can be found that the distribution of T_2 in CPMG and the projection of 2D T_1-T_2 map are consistent. The difference in the T_1/T_2 ratio is due to the deviation in T_1 distributions. T_1 relaxation in the 2D projection is shorter than measured by the 1D IR experiment. Principally, the spin relaxes during the recovery delay period τ_1 as well. Those spins in the vicinity of the paramagnetic centers will relax much faster. When detected by a CPMG train, it is likely that not all the signals can be refocused in the first π pulse, yielding a reduced measured T_1. A shorter spin echo might be able to alleviate this discrepancy, but this was experimentally very challenging due to ringing effects.

3.5 The effect of Fe(III) on the polymerization kinetics

3.5.1 T_2 time dependence *in situ*

The transverse relaxation during the curing period (72 hours) was recorded *in-situ* by a continuous CPMG train sequence. Figure 9 shows the evolution of T_2 (solid line) of MK0 during the curing. T_2 decreases with curing time and can be divided into three stages: (1) dissolution stage, (2) condensation stage, and (3) stabilization stage. In the dissolution stage, the starting material (metakaolin) was dissolved in the alkaline solution to form alumina/silica-hydroxyl species (monomers) without pore structures. Water was not confined and thus the spin relaxation was governed by the bulk relaxation mechanism. The measured T_2 of water at the beginning was 25 ms, much shorter than the bulk water relaxation (several seconds) and this is due to the high viscosity of the fresh paste. During this dissolution stage and after casting the material inside the mold its viscosity is increasing[46] and this resulted in the reduction of T_2 in the first ~ 2 hours. In the condensation stage, the dissolved monomers undergo a condensation polymerization and forms gels. The pore structures formed correspondingly, and water was confined inside them. T_2 changes dramatically in this stage from 10 ms to 0.6 ms due to the confinement of the water molecules inside the forming pores The relaxation mechanism of confined water follows the surface relaxation and molecular diffusion relaxation (beyond the fast diffusion regime)[47]. In the stabilization stage (after about 10 hours), stable chemical products and micro-structures have been formed, accompanied by minor local reorganization, keeping T_2 almost unchanged. In this last stage surface relaxation is dominating water spin relaxation (in the fast diffusion regime). The turning points between

the three stages were determined by calculating the 1st derivative of the T_2 curves. In the T_2 curve of MK0, the first turning point corresponding to the time when the pores start forming, occurred at 1.7 h after mixing, and the second turning point corresponding to the establishment of a stable pore structure, appeared at 10 h after mixing.

Calorimetry records the endothermic or exothermic process, which can correspond to chemical reactions or other thermal exchange processes such as wetting in the initial polymerization[48]. We have performed calorimetric measurements in situ and when compared to the cumulative heat release recorded by isothermal calorimetry (dashed line on Figure 9), we can observe also three stages as from the NMR relaxation measurements. The NMR measurements show the points three transitions more clearly. The time dependence of the T_2 relaxation times measured *in situ* provides complementary information about the pore formation during the geopolymerization.

3.5.2 The effect of Fe(III) ion on the T_2 evolution

Figure 10(a) shows the T_2 evolution of samples MK0 to MK8. In all graphs the same three evolution stages are visible within minor differences. During the dissolution stage, the presence of Fe(III) ions in the system reduces T_2 through the spin-electron dipole-dipole interactions. As shown in Figure 10(b), the transverse relaxation rate $1/T_2$ is linear dependent on Fe(III) content and becomes constant at higher Fe(III) content. Similar

behavior was also observed in a copper sulfate solution [49]. At higher Cu concentrations it was suggested that the aggregation of paramagnetic ions is causing this [48]. In solutions, a limited concentration of paramagnetic ions can be treated as a homogeneous dispersion and every paramagnetic center contributes to the dephasing of coherence. As the concentration rises, the paramagnetic ions aggregate to a larger size particle, which will reduce the contribution to the inhomogeneity of the fluctuating magnetic field and therefore the dephasing [50]. For the sample MK0 which contains no added Fe(III) the reduction in T_2 is induced by increasing viscosity, but this behavior is not observed for the other samples for which T_2 remains essentially constant upon introduction of Fe(III) ion to the systems (MK1-MK8). This is because the relaxation of movable water induced by the interaction with the surrounding Fe(III) ion is much faster than the relaxation caused by viscosity. To demonstrate that, we can compare the T_2 curves in MK0 and MK1, which should undergo a similar dissolution process. In MK0, T_2 decreases from 25 ms to 10 ms due to the increment in viscosity, while T_2 in MK1 is very short (only 1.6 ms) caused by the impact of Fe(III). So the viscosity-induced T_2 reduction can be exempted from assessment in MK1. In addition, the constant T_2 in MK1 and other samples is an indication that no fine pores have formed at this stage.

In the condensation stage, the behavior of the T_2 relaxation is more complicated, depending not only on the paramagnetic ion concentration but also on the formed pores. As a result, it is difficult to quantify the effect

of Fe(III) ion on T_2. However, we can still notice the changes in T_2 at the two turning points. For samples MK1-MK4 (see Figure 10(a-1)) the order in terms of decreasing T_2 values is the same between the first and the second turning points. As can be seen in Figure 10(a-2), for sample MK5-MK8 this order is different between the two turning points. This suggests that the samples with higher iron content generate larger pores under condensation, which is consistent with the 1D NMR and MICP results (see Figure 5). Moreover, the exact time moment when the first and the second turning points took place and the duration of the condensation stage were also dependent on the iron content, as shown in Figure 10(c). The first turning point takes place more or less at the same time for all samples, displaying a slight time delay with increasing iron content. This is attributed to the consumption of hydroxide ions by Fe(III), which reduced the dissolution rate. The exact time when the second turning point takes places follows a U-shape trend (Figure 10c). The same trend is also observed for the condensation stage duration which is likely related to the consumption of hydroxide ions by Fe(III) ions and the formation of Si(Al)-Fe co-precipitatess, which will be further analyzed in the discussion section.

In the stabilization stage, unlike the MK0 sample which displayed a steady T_2, all other samples experienced a slow increase in T_2 (in about 60 hours), which can be explained as the reorganization of the pore structures. Concretely, when the pores were just stabilized at the end of the condensation stage, the iron-based compound formed on the pore surface made the pore surface rough and thus increased the specific surface area

(S). According to Equation (2), T_2 is short when S is large. Over time, the iron precipitates started to aggregate and grew, reorganizing the pore into smaller S (smooth pore surface) and thus leading to the increase in T_2. The aggregates of iron also cause a longer T_2. Another possibility could be that water was transmitted from small pores towards the larger ones. However, such transport may be difficult due to capillary effects. Besides, we did not see an increase in T_2 for sample MK0, so this possibility could be excluded. Compared to the 7-day cured water-saturated samples (Figure 5(b)) where the measured T_2 is overall increased with iron content, the T_2 curves for the stabilization stage appeared to overlap in the high-iron content samples. Additionally, T_2 relaxation times are shorter than the ones measured with the 7-day cured samples. The reason can be that the water does not fully occupy the pore space in the freshly cured samples, resulting in T_2 being underestimated in the stabilization stage.

4. Discussion

In this section, we will discuss the causes of the pore size evolution with iron content. As shown in Fig 5(a), a threshold at the iron content of 2.0 wt% was found in the pore size evolution. The pore size increased slightly before the threshold and significantly after. The same threshold was observable in Figure 10(c), where the duration of the condensation stage experienced a U-shape curve with the iron content of 2.0 wt% defining its minimum value. We propose here possible explanations to describe this phenomenon. The hypothesis is that the threshold is related to the

consumption of hydroxide ions by Fe(III) and the formation of Fe oxyhydroxides. Ferrihydrite has been proposed as one of the Fe oxyhydroxide products and was produced by raising the pH of a ferric acid solution[51] similar to the alkaline environment in this work. The freshly produced ferrihydrite is poorly ordered and very active. Si-Fe co-precipitate will be formed as soon as SiO_4^{2-} ions are available, as this has been already reported in the literature[52]. In our work, the EDX spectra of MK8 illustrate that the Fe-rich phase contains a significant amount of Si and Al (Figure 11), which can be assigned as Si(Al)-Fe co-precipitate/complex. Such Si-Fe-O-containing phase was also observed by Perera *et. al* in the ferric nitrate-loaded geopolymers activated by sodium silicate solution with water-to-sodium ratio of 7.2:1[53].

The precipitation of Fe oxyhydroxides occurred at the very beginning during mixing. Released heat was observed during the manual mixing and was also detected as an exothermic peak in the first 20 min by isothermal calorimetry (see supplementary material figure S.1). The fresh precipitants would act as the nucleation seeds for the condensation of gels, which could accelerate the polymerization reaction rate[54]. On the contrary, the precipitation of Fe oxyhydroxides would consume the hydroxide ions, leading to the reduction in alkalinity and thus extending the condensation stage. When the iron content is below 2.0 wt%, the changes in alkalinity have little effect on the condensation and the resulting pore size. Previous research has shown that the same water/binder ratio and different NaOH/metakaolin (N/M) ratios resulted in a very similar pore diameter[55], which is consistent with the pore diameter changes (ranging

from 18.7 nm to 21.2 nm) in our work. When the iron content is above 2.0 wt%, the concentration of fresh Fe oxyhydroxides increases accordingly, providing the chance to form Si(Al) co-precipitate. The consumption of hydroxide ions, as well as the silicate and aluminum monomers, reduced the concentration of polymerization reactants and lead to the prolonged condensation stage. Decreased concentration of polymerization reactants could also lead to poor polymerization, resulting in larger pore sizes. The fresh precipitates, with a high specific surface (e.g., ferrihydrite with 600 m^2/g[51]), can act as an aggregate incorporated in the geopolymer matrix. This can increase the void rate in the matrix due to its large specific surface with a tendency for air retention[56].

The changes in pore sizes may also be related to the alteration in the Si/Al ratio in the geopolymer framework. The increase in Si/Al ratio resulted in a large decrease in the pore volume of geopolymers[57]. The introduction of Fe(III) ions can alter the Si/Al ratio by forming new clusters such as the co-precipitate discussed above, or by exchange with Al(III) in the geopolymer framework. Another possibility is that a proportion of the Fe(III) ion will act as the charge-balancing ion, similar to Na^+, but with a smaller size, which yields an increase in the pore size. As has been demonstrated by Steins *et. al*[4], the pore size, shape, and distribution of geopolymers depend on the size of alkali ions (charge balancing ions). All of these possibilities call for our attention to the role of iron in geopolymer structure, which needs further characterization.

5. Conclusions

The effect of paramagnetic Fe(III) ions on T_2 evolution in the early stage (first three days) of curing of MK-based geopolymers has been investigated for the first time to the best of our knowledge. Based on the T_2 time evolution curve, the polymerization process could be divided into three stages (i.e., dissolution, condensation and stabilization). The two turning points in the T_2 evolution indicated the time when the pores started to form and tended to stabilize. In the dissolution stage, the initial T_2 decayed with iron content. In the condensation stage, the effect of the Fe(III) ions on spin relaxation became complicated due to the combined relaxation mechanism. The presence of Fe(III) ions altered the duration of this stage. In the stabilization stage, the T_2 slightly increased only for the samples containing Fe(III).

The effect of Fe(III) ions on ^{1}H NMR relaxation has been studied via 1D T_1 and T_2, and 2D T_1-T_2 correlation experiments. The surface relaxivities (ρ_1 and ρ_2) exhibited linear correlation with iron content. In this work, ρ_1 and ρ_2 varied by about 1.5 times over the entire studied iron-content range. The paramagnetic Fe(III) ion has a less significant effect on NMR relaxation compared to the effect of increasing pore size. This might provide a foundation for the conversion of relaxation time to pore size for porous materials with soluble iron.

The introduction of soluble Fe(III) ion influenced the pore sizes after a threshold occurred at the iron content of 2.0 wt%. The same threshold has

also been found in the duration of the condensation stage in T_2 evolution curve. We proposed the possible reasons to explain this phenomenon that could be related to the consumption of hydroxides and the generation of Si-Fe complexes.

This work implies that it is possible to expand the application of LF NMR in iron-containing materials profiting from a lower paramagnetic effect compared to high field NMR studies. Limitations do remain of course when the iron content is high since the pore size measured by LF NMR may be underestimated due to the signal loss on the pore surface. The further investigation will include (a) investigation of the role of Fe(III) in geopolymer structure by techniques such as solid-state NMR, electron paramagnetic resonance (EPR), and Mössbauer spectroscopy, and (b) investigation of the influence of ferrous iron in geopolymer on both the NMR response and the geopolymer structure.

Acknowledgment

This project was supported by the KU Leuven Grant STG-18-00289 and by the Research Foundation Flanders (FWO) under Grant PorMedNMR − No. G0D5419N.

References:

[1] J. Davidovits, Geopolymers, Journal of thermal analysis, 37 (1991) 1633-1656, https://doi.org/10.1007/BF01912193.

[2] A. Bakri, H. Kamarudin, M. Binhussain, I.K. Nizar, A. Rafiza, Y. Zarina, Comparison of geopolymer fly ash and ordinary portland cement to the strength of concrete, Advanced Science Letters, 19 (2013) 3592-3595, https://doi.org/10.1166/asl.2013.5187.

[3] C. Maitland, C. Buckley, B. O'connor, P. Butler, R. Hart, Characterization of the pore structure of metakaolin-derived geopolymers by neutron scattering and electron microscopy, Journal of Applied Crystallography, 44 (2011) 697-707, https://doi.org/10.1107/S0021889811021078.

[4] P. Steins, A. Poulesquen, F. Frizon, O. Diat, J. Jestin, J. Causse, D. Lambertin, S. Rossignol, Effect of aging and alkali activator on the porous structure of a geopolymer, Journal of Applied Crystallography, 47 (2014) 316-324, https://doi.org/10.1107/S160057671303197X.

[5] J. Li, S. Mailhiot, H. Sreenivasan, A.M. Kantola, M. Illikainen, E. Adesanya, L. Kriskova, V.-V. Telkki, P. Kinnunen, Curing process and pore structure of metakaolin-based geopolymers: Liquid-state 1H NMR investigation, Cement and Concrete Research, 143 (2021) 106394, https://doi.org/10.1016/j.cemconres.2021.106394.

[6] Z. Farhana, H. Kamarudin, A. Rahmat, M.M. Al Bakri Abdullah, S. Norainiza, Corrosion performance of reinforcement bar in geopolymer concrete compare with its performance in ordinary portland cement concrete: a short review, Advanced Materials Research, Trans Tech Publ, 2013, pp. 509-512.

[7] K. Lyu, W. She, C. Miao, H. Chang, Y. Gu, Quantitative characterization of pore morphology in hardened cement paste via SEM-BSE image analysis, Construction and Building Materials, 202 (2019) 589-602, https://doi.org/10.1016/j.conbuildmat.2019.01.055.

[8] J. Kaufmann, R. Loser, A. Leemann, Analysis of cement-bonded materials by multi-cycle mercury intrusion and nitrogen sorption, Journal of Colloid and Interface Science, 336 (2009) 730-737, https://doi.org/10.1016/j.jcis.2009.05.029.

[9] Y. Wang, Q. Yuan, D. Deng, T. Ye, L. Fang, Measuring the pore structure of cement asphalt mortar by nuclear magnetic resonance, Construction and building materials, 137 (2017) 450-458, https://doi.org/10.1016/j.conbuildmat.2017.01.109.

[10] L. Liu, Z. He, X. Cai, S. Fu, Application of Low-Field NMR to the Pore Structure of Concrete, Applied Magnetic Resonance, 52 (2021) 15-31, https://doi.org/10.1007/s00723-020-01229-7.

[11] J. Bisschop, J.G.M. Van Mier, Drying Shrinkage Microcracking in Cement-based Materials, Heron, 47 (3), 2002, (2002),
[12] P. Zhang, S. Lu, J. Li, J. Zhang, H. Xue, C. Chen, Comparisons of SEM, Low-Field NMR, and Mercury Intrusion Capillary Pressure in Characterization of the Pore Size Distribution of Lacustrine Shale: A Case Study on the Dongying Depression, Bohai Bay Basin, China, Energy & Fuels, 31 (2017) 9232-9239, https://doi.org/10.1021/acs.energyfuels.7b01625.
[13] C. Lyu, Z. Ning, Q. Wang, M. Chen, Application of NMR T2 to Pore Size Distribution and Movable Fluid Distribution in Tight Sandstones, Energy & Fuels, 32 (2018) 1395-1405, https://doi.org/10.1021/acs.energyfuels.7b03431.
[14] X. Li, Y. Li, C. Chen, D. Zhao, X. Wang, L. Zhao, H. Shi, G. Ma, Z. Su, Pore size analysis from low field NMR spin–spin relaxation measurements of porous microspheres, Journal of Porous Materials, 22 (2015) 11-20, https://doi.org/10.1007/s10934-014-9864-x.
[15] C. Cadar, A. Cretu, M. Moldovan, C. Mattea, S. Stapf, I. Ardelean, NMR T1–T2 correlation analysis of molecular absorption inside a hardened cement paste containing silanised silica fume, Molecular Physics, 117 (2019) 1000-1005, https://doi.org/10.1080/00268976.2018.1513582.
[16] X. Yuan, G. Liao, In situ characterization of early-age hydration process of recycled powder blended cement paste using low-field NMR, Fullerenes, Nanotubes and Carbon Nanostructures, (2021) 1-8, https://doi.org/10.1080/1536383X.2021.1917554.
[17] J. Keeler, Understanding NMR spectroscopy, John Wiley & Sons, Chichester, 2011.
[18] K.-J. Dunn, D.J. Bergman, G.A. Latorraca, K. Helbig, S. Treitel, Handbook of Geophysical Exploration, Pergamon, 2002.
[19] K.R. Brownstein, C.E. Tarr, Importance of classical diffusion in NMR studies of water in biological cells, Physical Review A, 19 (1979) 2446-2453, https://doi.org/10.1103/PhysRevA.19.2446.
[20] K. Keating, R. Knight, A laboratory study of the effect of magnetite on NMR relaxation rates, Journal of Applied Geophysics, 66 (2008) 188-196, https://doi.org/10.1016/j.jappgeo.2007.09.001.
[21] F. Jaeger, S. Bowe, H. Van As, G. Schaumann, Evaluation of 1H NMR relaxometry for the assessment of pore-size distribution in soil samples, European Journal of Soil Science, 60 (2009) 1052-1064, https://doi.org/10.1111/j.1365-2389.2009.01192.x.
[22] M. Karatas, M. Dener, M. Mohabbi, A. Benli, A study on the compressive strength and microstructure characteristic of alkali-activated metakaolin cement, Matéria (Rio de Janeiro), 24 (2019), https://doi.org/10.1590/S1517-707620190004.0832.
[23] M. Narmatha, T. Felixkala, Analyse the mechanical properties of metakaolin using as a partial replacement of cement in concrete, Educational Research Institute University, Chennai,

India, (2017), https://doi.org/10.14445/23488352/IJCE-V4I1P103.
[24] A.S. Tarasov, E.P. Kearsley, A.S. Kolomatskiy, H.F. Mostert, Heat evolution due to cement hydration in foamed concrete, Magazine of Concrete Research, 62 (2010) 895-906, https://doi.org/10.1680/macr.2010.62.12.895.
[25] D.W. Law, A.A. Adam, T.K. Molyneaux, I. Patnaikuni, A. Wardhono, Long term durability properties of class F fly ash geopolymer concrete, Materials and Structures, 48 (2015) 721-731, https://doi.org/10.1617/s11527-014-0268-9.
[26] T. Hertel, B. Blanpain, Y. Pontikes, A Proposal for a 100 % Use of Bauxite Residue Towards Inorganic Polymer Mortar, Journal of Sustainable Metallurgy, 2 (2016) 394-404, https://doi.org/10.1007/s40831-016-0080-6.
[27] I. Foley, S.A. Farooqui, R.L. Kleinberg, Effect of Paramagnetic Ions on NMR Relaxation of Fluids at Solid Surfaces, Journal of Magnetic Resonance, Series A, 123 (1996) 95-104, https://doi.org/10.1006/jmra.1996.0218.
[28] R.L. Kleinberg, W.E. Kenyon, P.P. Mitra, Mechanism of NMR Relaxation of Fluids in Rock, Journal of Magnetic Resonance, Series A, 108 (1994) 206-214, https://doi.org/10.1006/jmra.1994.1112.
[29] J. Korringa, D.O. Seevers, H.C. Torrey, Theory of Spin Pumping and Relaxation in Systems with a Low Concentration of Electron Spin Resonance Centers, Physical Review, 127 (1962) 1143-1150, https://doi.org/10.1103/PhysRev.127.1143.
[30] R. Schulte Holthausen, M. Raupach, A phenomenological approach on the influence of paramagnetic iron in cement stone on 2D T1-T2 relaxation in single-sided 1H nuclear magnetic resonance, Cement and Concrete Research, 120 (2019) 279-293, https://doi.org/10.1016/j.cemconres.2019.03.027.
[31] T.R. Bryar, C.J. Daughney, R.J. Knight, Paramagnetic Effects of Iron(III) Species on Nuclear Magnetic Relaxation of Fluid Protons in Porous Media, Journal of Magnetic Resonance, 142 (2000) 74-85, https://doi.org/10.1006/jmre.1999.1917.
[32] P.J. McDonald, J.P. Korb, J. Mitchell, L. Monteilhet, Surface relaxation and chemical exchange in hydrating cement pastes: A two-dimensional NMR relaxation study, Physical Review E, 72 (2005) 011409, https://doi.org/10.1103/PhysRevE.72.011409.
[33] K. Vijai, R. Kumutha, B. Vishnuram, Effect of types of curing on strength of geopolymer concrete, International journal of physical sciences, 5 (2010) 1419-1423, http://dx.doi.org/10.12989/acc.2014.2.1.029.
[34] P. Rovnaník, Effect of curing temperature on the development of hard structure of metakaolin-based geopolymer, Construction and building materials, 24 (2010) 1176-1183, https://doi.org/10.1016/j.conbuildmat.2009.12.023.

[35] A. Pop, C. Badea, I. Ardelean, The effects of different superplasticizers and water-to-cement ratios on the hydration of gray cement using T 2-NMR, Applied Magnetic Resonance, 44 (2013) 1223-1234, https://doi.org/10.1007/s00723-013-0475-5.
[36] X. Cong, W. Zhou, X. Geng, M. Elchalakani, Low field NMR relaxation as a probe to study the effect of activators and retarders on the alkali-activated GGBFS setting process, Cement and Concrete Composites, 104 (2019) 103399, https://doi.org/10.1016/j.cemconcomp.2019.103399.
[37] F. Barberon, J.P. Korb, D. Petit, V. Morin, E. Bermejo, Probing the Surface Area of a Cement-Based Material by Nuclear Magnetic Relaxation Dispersion, Physical Review Letters, 90 (2003) 116103, 10.1103/PhysRevLett.90.116103.
[38] D.S. Perera, J.D. Cashion, M.G. Blackford, Z. Zhang, E.R. Vance, Fe speciation in geopolymers with Si/Al molar ratio of∼ 2, Journal of the European Ceramic Society, 27 (2007) 2697-2703, https://doi.org/10.1016/j.jeurceramsoc.2006.10.006.
[39] P.A. Schroeder, R.J. Pruett, Fe ordering in kaolinite; insights from 29Si and 27Al MAS NMR spectroscopy, American Mineralogist, 81 (1996) 26-38, https://doi.org/10.2138/am-1996-1-204.
[40] C. Voigt, J. Hubálková, H. Giesche, C.G. Aneziris, Intrusion and extrusion mercury porosimetry measurements at Al2O3–C - Influence of measuring parameter, Microporous and Mesoporous Materials, 299 (2020) 110125, https://doi.org/10.1016/j.micromeso.2020.110125.
[41] K. Keating, R. Knight, A laboratory study of the effect of Fe (II)-bearing minerals on nuclear magnetic resonance (NMR) relaxation measurements, Geophysics, 75 (2010) F71-F82,
[42] P. Mesquita, A. Souza, G. Carneiro, A. Boyd, F. Ferreira, P. Machado, V. Anand, L. Schwartz, Surface relaxivity estimation and NMR-MICP matching in diffusionaly coupled rocks, International Symposium of the Society of Core Analysts, Snowmass, Colorado, 2016, pp. 21-26.
[43] F. Dalas, J.-P. Korb, S. Pourchet, A. Nonat, D. Rinaldi, M. Mosquet, Surface Relaxivity of Cement Hydrates, The Journal of Physical Chemistry C, 118 (2014) 8387-8396, https://doi.org/10.1021/jp500055p.
[44] C. Naber, F. Kleiner, F. Becker, L. Nguyen-Tuan, C. Rößler, M.A. Etzold, J. Neubauer, C-S-H Pore Size Characterization Via a Combined Nuclear Magnetic Resonance (NMR)–Scanning Electron Microscopy (SEM) Surface Relaxivity Calibration, Materials, 13 (2020) 1779, https://doi.org/10.3390/ma13071779.
[45] C. D'Agostino, P. Bräuer, P. Charoen-Rajapark, M.D. Crouch, L.F. Gladden, Effect of paramagnetic species on T 1, T 2 and T 1/T 2 NMR relaxation times of liquids in porous CuSO 4/Al 2 O 3, RSC Advances, 7 (2017) 36163-36167, https://doi.org/10.1039/C7RA07165E

[46] A. Poulesquen, F. Frizon, D. Lambertin, Rheological behavior of alkali-activated metakaolin during geopolymerization, Journal of Non-Crystalline Solids, 357 (2011) 3565-3571, https://doi.org/10.1016/j.jnoncrysol.2011.07.013.
[47] P. Porion, A. Delville, A Multi-Scale Study of Water Dynamics under Confinement, Exploiting Numerical Simulations in Relation to NMR Relaxometry, PGSE and NMR Micro-Imaging Experiments: An Application to the Clay/Water Interface, International Journal of Molecular Sciences, 21 (2020) 4697, https://doi.org/10.3390/ijms21134697.
[48] S. Pilehvar, S.G. Sanfelix, A.M. Szczotok, J.F. Rodríguez, L. Valentini, M. Lanzón, R. Pamies, A.-L. Kjøniksen, Effect of temperature on geopolymer and Portland cement composites modified with Micro-encapsulated Phase Change materials, Construction and Building Materials, 252 (2020) 119055, https://doi.org/10.1016/j.conbuildmat.2020.119055.
[49] L.L. Barbosa, L.A. Colnago, I. Carlos, L. M. S. Nunes, Low-Field NMR-Electrochemical Cell For In Situ Measurements of Paramagnetic Species, ECS Transactions, 25 (2010) 215-221, https://doi.org/10.1149/1.3334810.
[50] R.N. Muller, P. Gillis, F. Moiny, A. Roch, Transverse relaxivity of particulate MRI contrast media: from theories to experiments, Magnetic resonance in medicine, 22 (1991) 178-182, https://doi.org/10.1002/mrm.1910220203.
[51] T.E. Payne, G.R. Lumpkin, T.D. Waite, Chapter 2 - UraniumVI Adsorption on Model Minerals: Controlling Factors and Surface Complexation Modeling, in: E.A. Jenne (Ed.) Adsorption of Metals by Geomedia, Academic Press, San Diego, 1998, pp. 75-97.
[52] A.M. Jones, R.N. Collins, J. Rose, T.D. Waite, The effect of silica and natural organic matter on the Fe(II)-catalysed transformation and reactivity of Fe(III) minerals, Geochimica et Cosmochimica Acta, 73 (2009) 4409-4422, https://doi.org/10.1016/j.gca.2009.04.025.
[53] D.S. Perera, J.D. Cashion, M.G. Blackford, Z. Zhang, E.R. Vance, Fe speciation in geopolymers with Si/Al molar ratio of ~2, Journal of the European Ceramic Society, 27 (2007) 2697-2703, https://doi.org/10.1016/j.jeurceramsoc.2006.10.006.
[54] L. Prasittisopin, I. Sereewatthanawut, Effects of seeding nucleation agent on geopolymerization process of fly-ash geopolymer, Frontiers of Structural and Civil Engineering, 12 (2018) 16-25, https://doi.org/10.1007/s11709-016-0373-7.
[55] S. Park, M. Pour-Ghaz, What is the role of water in the geopolymerization of metakaolin?, Construction and Building Materials, 182 (2018) 360-370, https://doi.org/10.1016/j.conbuildmat.2018.06.073.
[56] S. Chuah, W.H. Duan, Z. Pan, E. Hunter, A.H. Korayem, X.L. Zhao, F. Collins, J.G. Sanjayan, The properties of fly ash based

geopolymer mortars made with dune sand, Materials & Design, 92 (2016) 571-578, https://doi.org/10.1016/j.matdes.2015.12.070.

[57] P. Duxson, J.L. Provis, G.C. Lukey, S.W. Mallicoat, W.M. Kriven, J.S.J. van Deventer, Understanding the relationship between geopolymer composition, microstructure and mechanical properties, Colloids and Surfaces A: Physicochemical and Engineering Aspects, 269 (2005) 47-58, https://doi.org/10.1016/j.colsurfa.2005.06.060.

Tables

Table 1. Chemical composition of metakaolin

Chemicals	Al_2O_3	SiO_2	TiO_2	Fe_2O_3	Others
wt%	46.0	50.9	2.5	0.3	0.3

Table 2. Chemicals used for preparing geopolymer samples

Samples and chemicals[a]									
	MK0	MK1	MK2	MK3	MK4	MK5	MK6	MK7	MK8
Fe content* (wt%)	0	0.5	1.0	1.5	2.0	2.5	3.0	3.5	4.0
Metakaolin (g)	3.0								
$FeCl_3$ concentration (g/mL)	0	0.073	0.145	0.218	0.290	0.363	0.435	0.508	0.580
$FeCl_3$ (mL)	0.5								
Calculated components[b]									
Total H_2O (g)	2.81	2.80	2.78	2.77	2.76	2.75	2.74	2.72	2.71
Water/binder ratio (g/g)	0.388	0.387	0.386	0.385	0.384	0.383	0.382	0.381	0.380

*The concentration of iron was calculated as the percentage of Fe(III) ion added to metakaolin. For instance, 0.5 wt% iron meant 0.015 g Fe(III) ion, originated from the loaded $FeCl_3$ solution, was added to 3 g metakaolin powder.

[a]In all cases, metakaolin powder was mixed with $FeCl_3$ solution thoroughly before mixing with the alkaline solution to avoid the iron aggregate. All the reactants were mixed at room temperature for 15 min before being transferred to the oven/NMR chamber.

[b]The amount of water was calculated as the total water in the alkaline activator and the $FeCl_3$ solution. The alterations in water amount and the water/binder ratio were due to the different concentrations of $FeCl_3$ solutions.

Figures

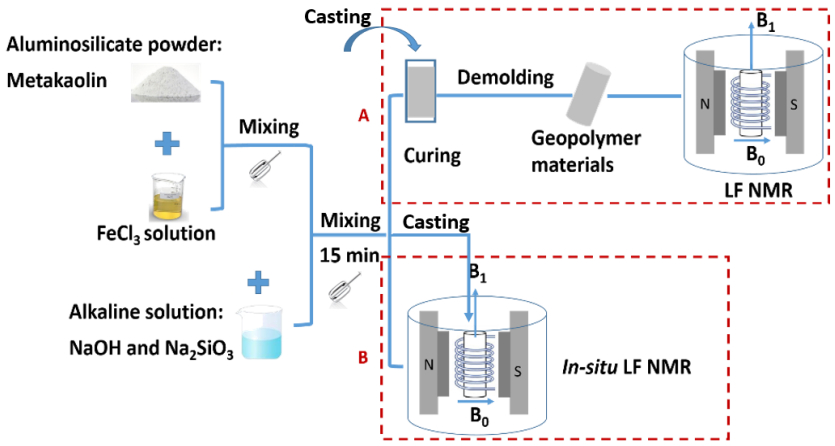

Figure 1. Scheme of the experimental procedures. Metakaolin geopolymers loaded with various amounts of Fe(III) were synthesized by mixing metakaolin with $FeCl_3$ solutions and alkaline activators. (A) The mixtures were cast into a silicone mold and cured for 20h at 40°C, followed by the LF NMR measurements (1D T_1 and T_2 relaxation times and 2D T_1 - T_2 correlations) after demolding. (B) The mixtures were loaded into an NMR Teflon mold and immediately transferred into the closed NMR chamber to *in-situ* record the T_2 relaxation time during the curing period (28°C).

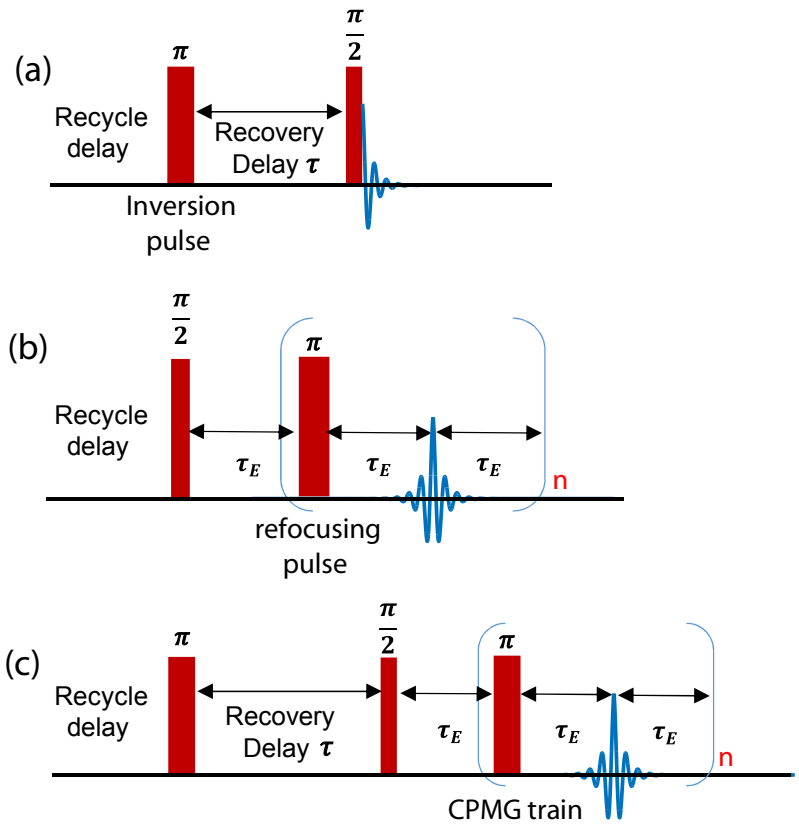

Figure 2 (a) Inversion – recovery pulse sequence used for the measurement of T_1 relaxation. The recovery delay τ was set to 15 logarithmic values and the recycle delay to 5 s; (b) CPMG pulse sequence used for the measurement of T_2 relaxation. The sequence parameters were set as: number of echoes n = 5000, echo time $2\tau_E$ = 160 μs, $\frac{\pi}{2}$ pulse length = 8.2 μs, recycle delay = 3 s; (c) The pulse sequence used for 2D T_1-T_2 correlation experiments. The NMR signal were collected for 14 logarithmic values of τ, n = 6000, $2\tau_E$ = 190 μs, recycle delay = 3 s.

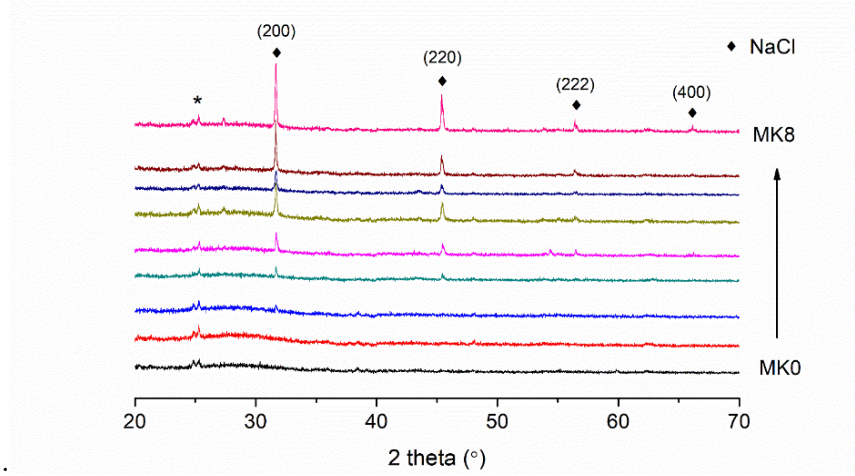

Figure 3 XRD diffractograms of geopolymers from MK0 to MK8. The diamond symbols represent the characteristic NaCl peaks while the star indicates an anatase impurity.

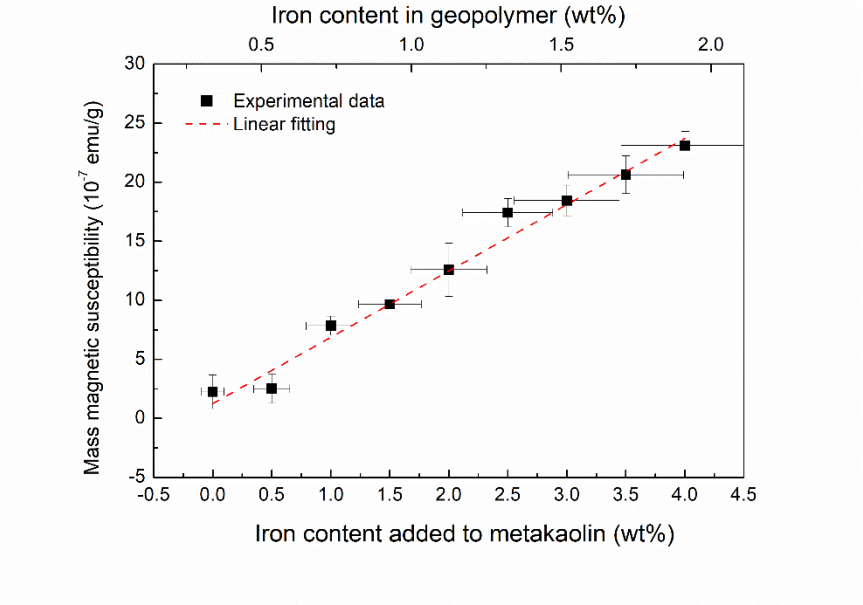

Figure 4 Mass magnetic susceptibility versus the iron content. The dashed line is fitted by a linear curve. The iron contents in the bottom x-axis is the mass ratio of Fe(III) added in metakaolin. The iron contents in upper x-axis have been calculated from the mass ratio of Fe(III) in the final geopolymer samples.

(a)

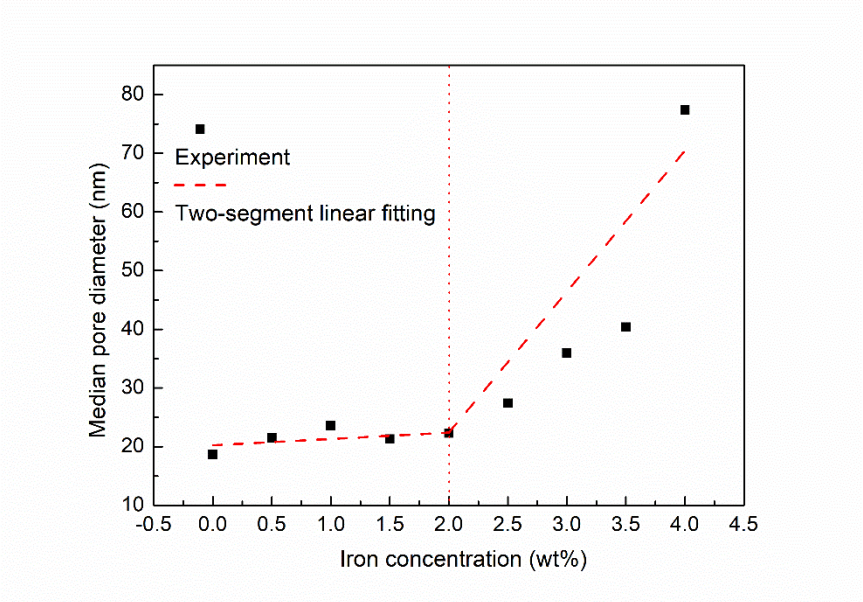
Median pore diameter (nm)
Iron concentration (wt%)
Experiment
Two-segment linear fitting
10
20
30
40
50
60
70
80
-0.5
0.0
0.5
1.0
1.5
2.0
2.5
3.0
3.5
4.0
4.5

(b)

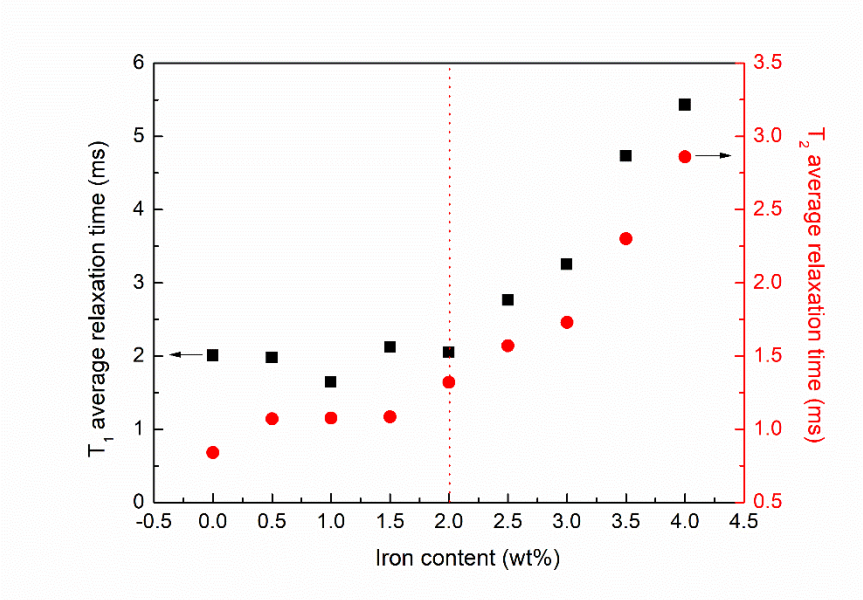
T1 average relaxation time (ms)
T2 average relaxation time (ms)
Iron content (wt%)
0
1
2
3
4
5
6
0.5
1.0
1.5
2.0
2.5
3.0
3.5
-0.5
0.0
0.5
1.0
1.5
2.0
2.5
3.0
3.5
4.0
4.5

(c)

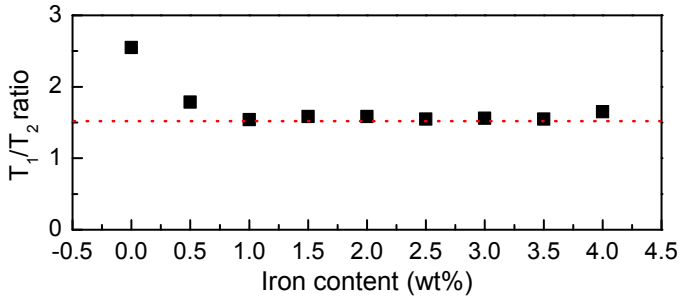

Figure 5 (a) Median pore diameter (r_{50}) versus iron content determined by MICP. (b) Longitudinal (black dot) and transverse (red dot) relaxation time versus iron concentration. (c) The T_1/T_2 ratio is calculated from (b).

(a)

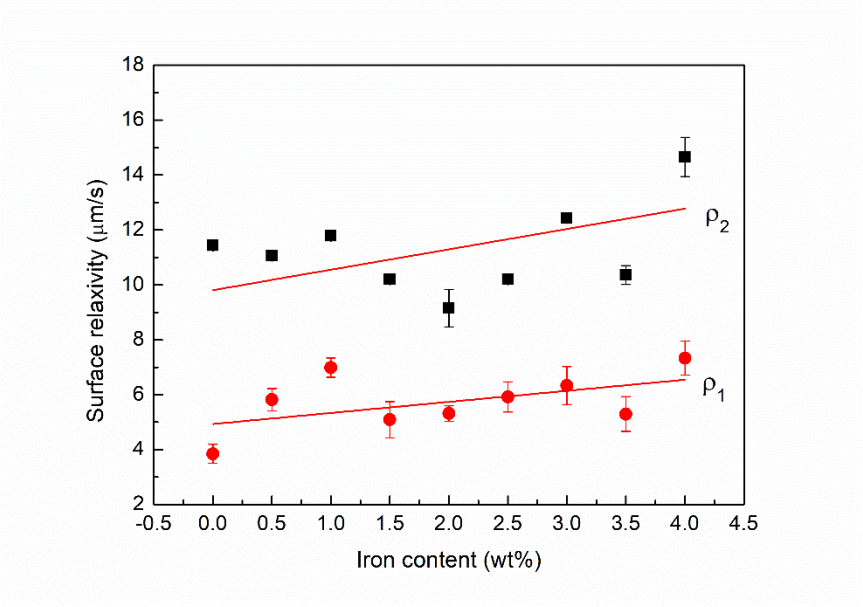

(b)

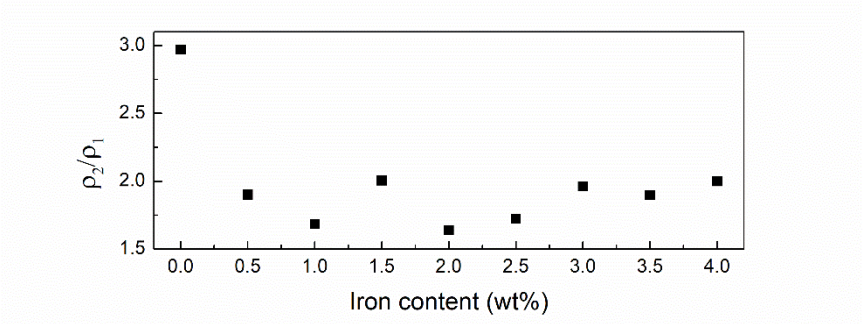

Figure 6 (a) Longitudinal (red circles) and transverse (black squares) surface relaxivities for the geopolymers versus iron content. The data are fitted with a straight line. (b) Calculated ρ_2/ρ_1 ratio.

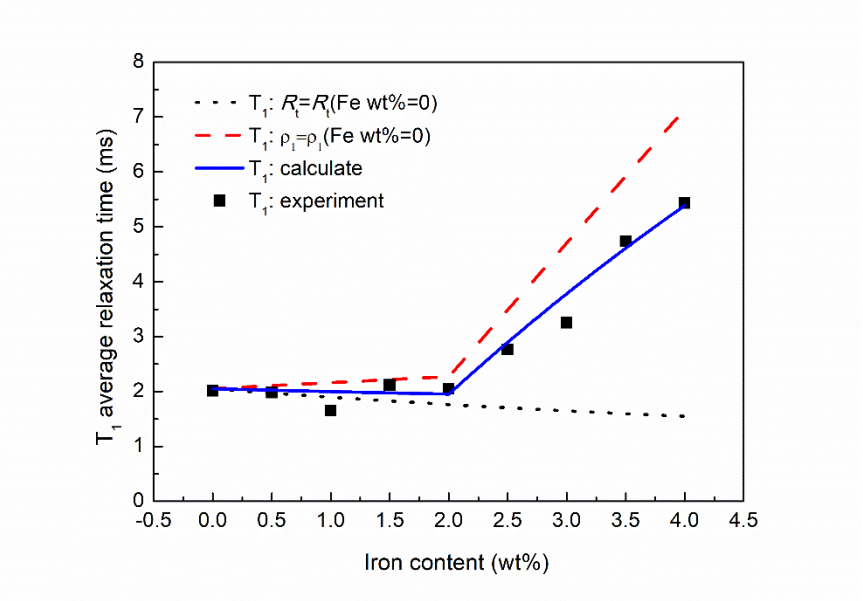

Figure 7 Schematic plot of the evolution of longitudinal relaxation times with iron content.

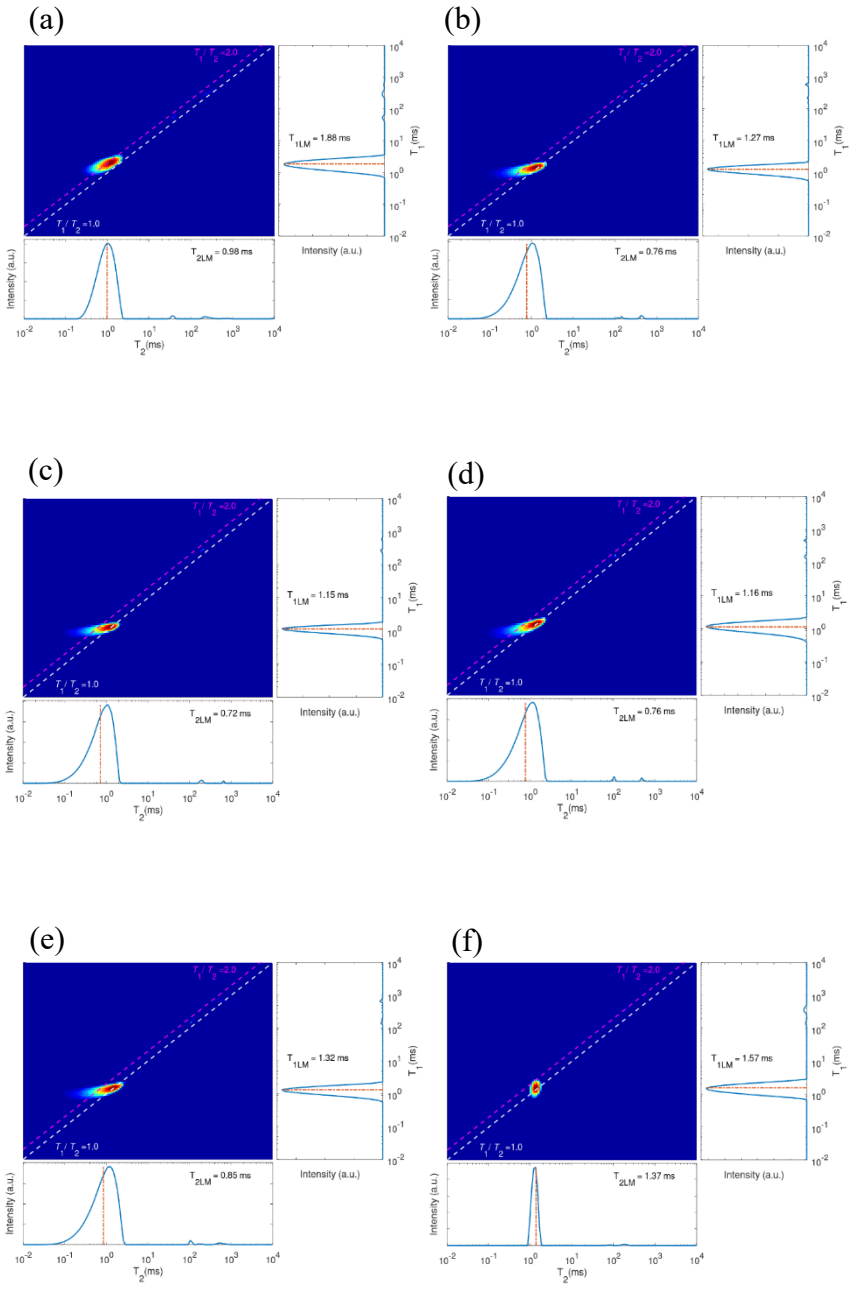
(a)
(b)
(c)
(d)
(e)
(f)
T1 / T2 =2.0
T1 / T2 =1.0
T1LM = 1.88 ms
T2LM = 0.98 ms
T1LM = 1.27 ms
T2LM = 0.76 ms
T1LM = 1.15 ms
T2LM = 0.72 ms
T1LM = 1.16 ms
T2LM = 0.76 ms
T1LM = 1.32 ms
T2LM = 0.85 ms
T1LM = 1.57 ms
T2LM = 1.37 ms
Intensity (a.u.)
T1 (ms)
T2 (ms)

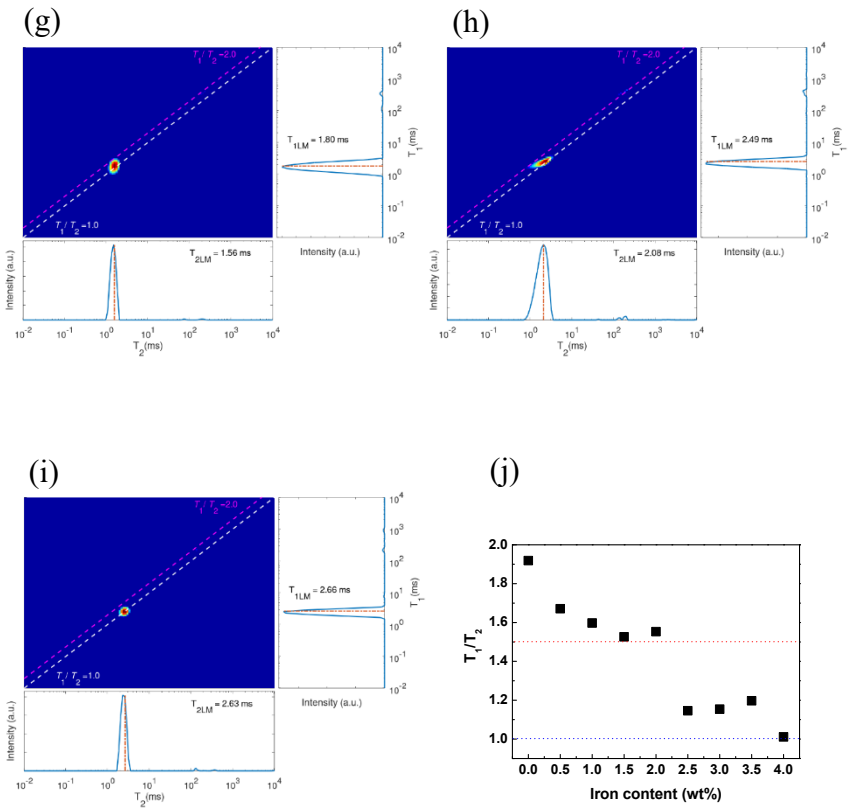

Figure 8 2D maps of T_1 - T_2 correlation correspond to adding additional iron with (a) 0 % (MK0), (b) 0.5 wt% (MK1), (c) 1.0 wt% (MK2), (d) 1.5 wt% (MK3), (e) 2.0 wt% (MK4), (f) 2.5 wt% (MK5), (g) 3.0 wt% (MK6), (h) 3.5 wt% (MK7), and (i) 4.0 wt% (MK8). The T_1/T_2 ratio in (j) was calculated from the 2D maps.

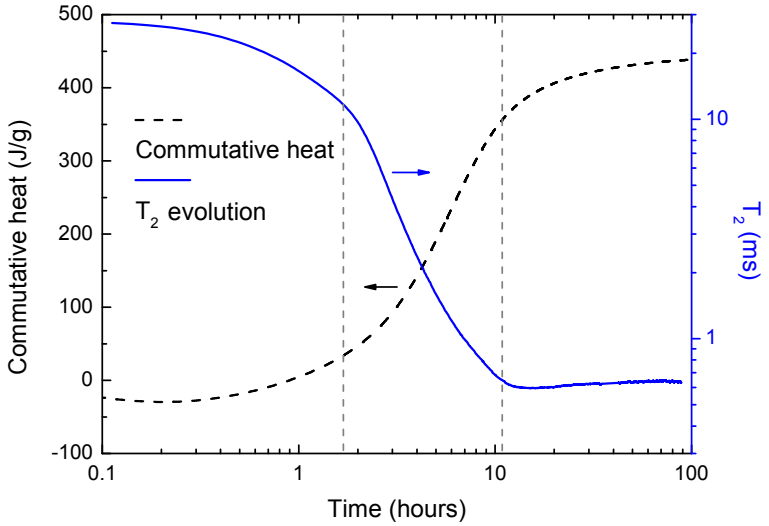

Figure 9 Time evolution of T_2 (black line) and heat (blue line) in the early stage (first three days) of geopolymerization.

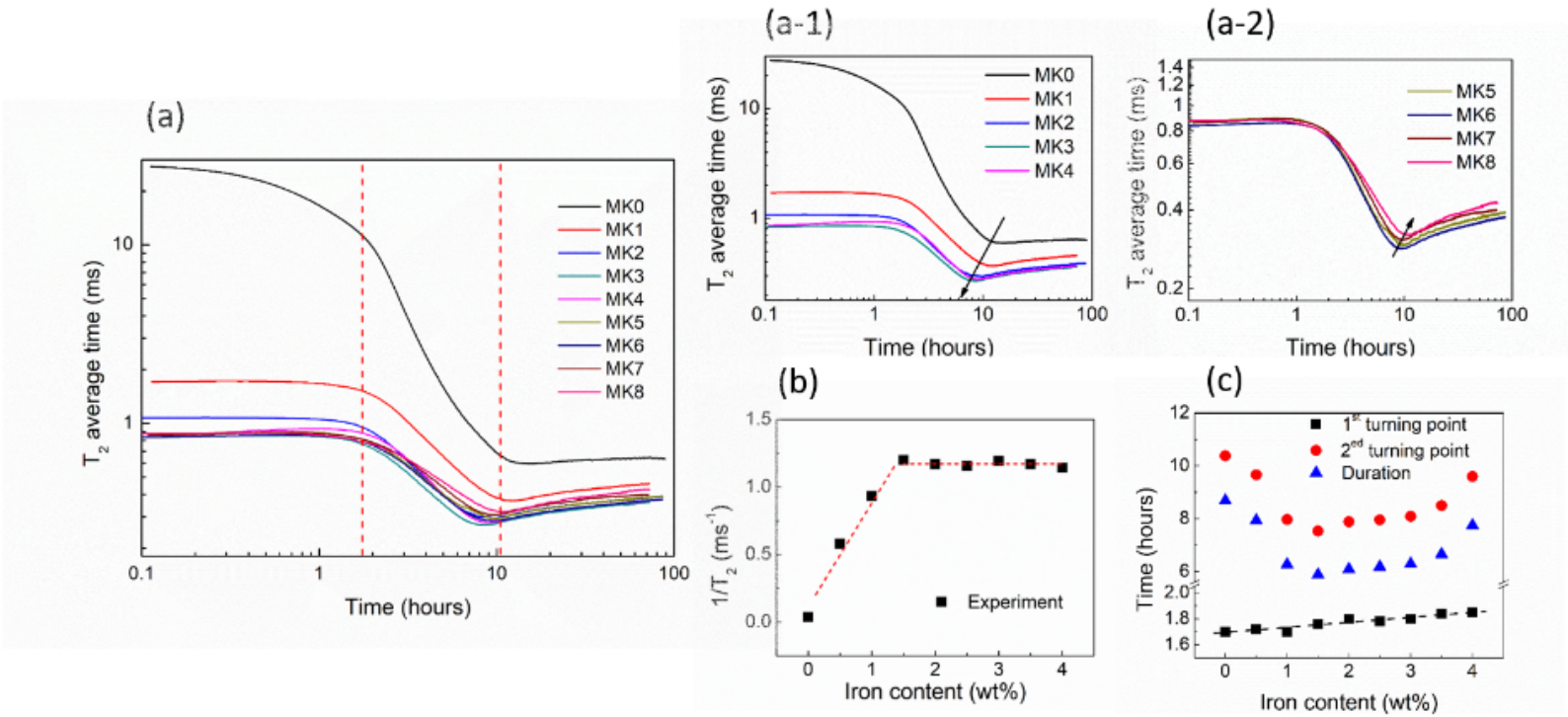
(a)
T2 average time (ms)
Time (hours)
MK0
MK1
MK2
MK3
MK4
MK5
MK6
MK7
MK8
(a-1)
(a-2)
(b)
1/T2 (ms-1)
Experiment
Iron content (wt%)
(c)
Time (hours)
1st turning point
2nd turning point
Duration

Figure 10 (a) T_2 average time evolution in the early stage (first 3 days) of polymerization in MK-based geopolymers. (a-1) and (a-2) separate the two groups of samples. (b) Initial (time = 0) transverse relaxation time as a function of iron content. (c) Evolution of turning points and condensation stage duration with iron content.

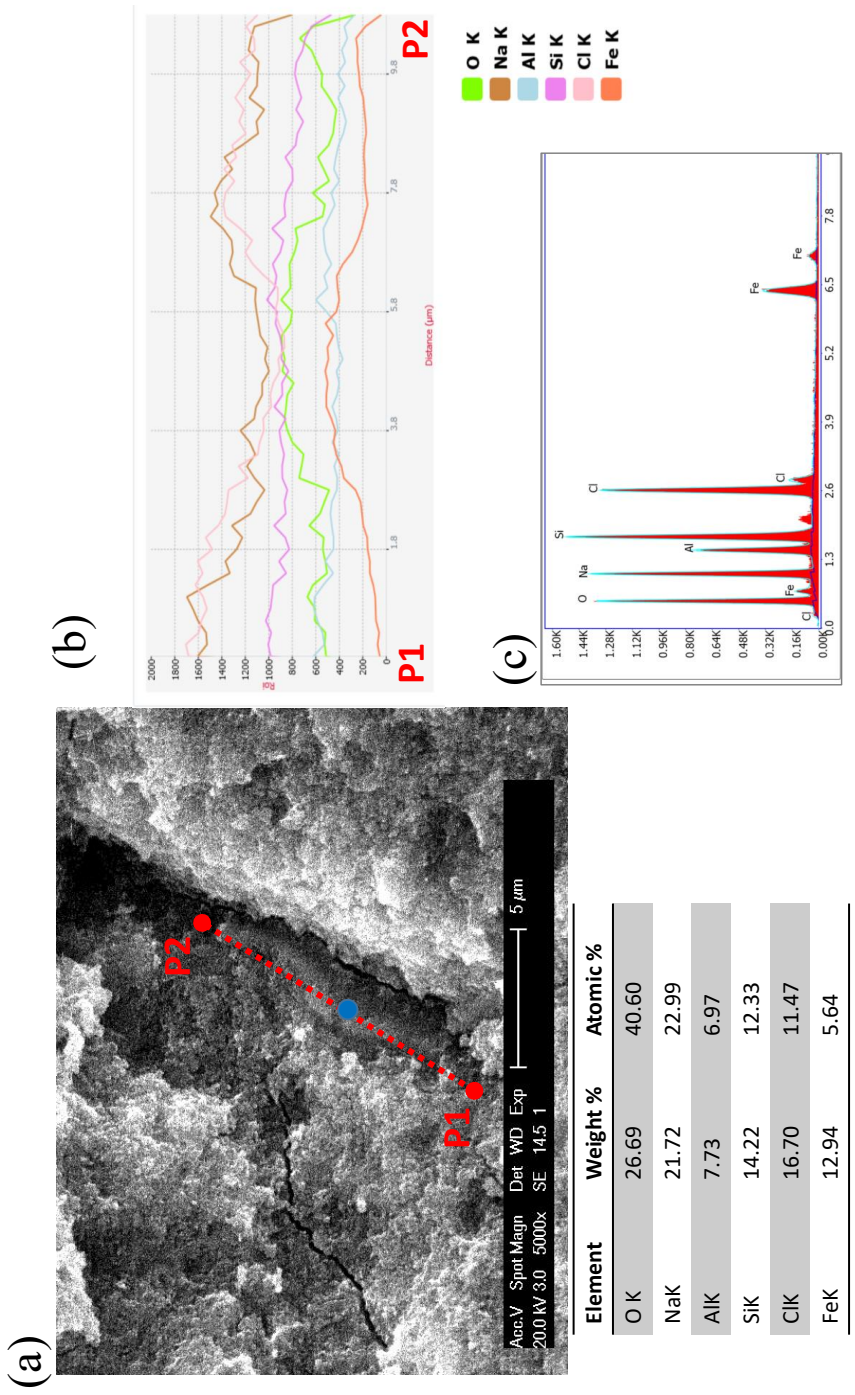

Element	Weight %	Atomic %
O K	26.69	40.60
NaK	21.72	22.99
AlK	7.73	6.97
SiK	14.22	12.33
ClK	16.70	11.47
FeK	12.94	5.64

Figure 11 (a) SEM of the cross-section of MK8. (b) The X-ray line scanning area relates to the red dash line in SEM, P1 and P2 represent

the beginning and end scanning points on (a). (c) The EDX spectrum and the element composition corresponding to the blue point in the SEM graph.